Asian Journal of Chemistry; Vol. 37, No. 7 (2025), 1690-1696

ASIAN JOURNAL OF CHEMISTRY

https://doi.org/10.14233/ajchem.2025.33918

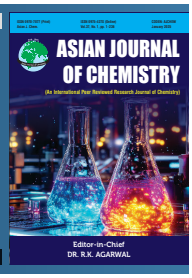

Enhanced Electrochemical Performance of Cobalt-Substituted Zinc Ferrite for High-Stability Supercapacitors

S. ANBUKARUPPUCHAMY[1,*], P. BALAMURUGAN[1], P. VIJAYAMATHUBALAN[1], JANET DAYANITHI[2] and J. VIDYA[3]

[1]Department of Physics, Government Arts College, Nandanam, Chennai-600035, India
[2]Department of Chemistry, School of Basic Science, VISTAS, Pallavaram, Chennai-600117, India
[3]Department of Physics, Arignar Anna Government Arts College, Namakkal-637002, India

*Corresponding author: E-mail: loveaksamy@gmail.com

Received: 9 May 2025; *Accepted*: 10 June 2025; *Published online*: 30 June 2025; AJC-22044

Cobalt-substituted zinc ferrite ($Co_xZn_{1-x}Fe_2O_4$) nanoparticles were synthesized and studied for their structural, morphological and electrochemical properties. The XRD results confirmed that the prepared samples possess cubic spinel structure with crystallite size decreased from 31.45 nm to 26.13 nm upon cobalt substitution. FTIR and Raman spectroscopic studies validated spinel phase formation with metal-oxygen vibrations in tetrahedral and octahedral sites. The FESEM study showed agglomerated morphology and the EDX result confirmed stoichiometry. Electrochemical tests (CV, GCD, EIS, cyclic stability test) revealed improved charge storage and conductivity caused by cobalt content. $Co_{0.5}Zn_{0.5}Fe_2O_4$ achieved 306.2 F/g at 1 A/g and 96% capacitance retention after 4000 cycles at 10 A/g, indicating its potential as a high-performance supercapacitor electrode.

Keywords: Supercapacitor, Cubic spinel structure, Electrochemical energy storage, Charge transfer kinetics.

INTRODUCTION

The global energy demand is rising due to rapid industrialization, population growth and technological progress. This demand has traditionally been met using non-renewable, fossil fuels like coal, oil and natural gas. To ensure sustainability, there is a growing focus on clean, renewable energy sources such as solar, wind, hydro and geothermal, biomass and efficient energy storage and conversion technologies. Among storage solutions, fuel cells, batteries and supercapacitors play key roles, each suited to different applications [1,2]. Comparing other storage technologies supercapacitors offer rapid charge/discharge capabilities, high power handling capacity and long cycle life due to their surface storage mechanism [3]. Based on their charge storage mechanisms, the electric double-layer capacitors (EDLCs) store energy through electrostatic adsorption using inert materials like carbon. At the same time, the pseudocapacitors rely on fast Faradaic redox reactions involving active materials [4,5].

Transition metal oxides are considered promising materials for supercapacitor electrodes due to their high specific capacitance and efficient charge transfer abilities [6,7]. Nowadays, developing complex metal oxide-based materials that are both inexpensive and possess high specific capacitance is highly desirable. In addition, transition metal oxides possess spinel structures, such as spinel ferrites (MFe_2O_4, M = Fe, Co, Ni, Mn, Cu, Zn) are well suited for energy storage and conversion technologies due to their rich redox states and capability to exhibit electrochemical stability. Feng *et al.* [8] investigated the capacitance of $NiFe_2O_4$ nanoparticles, which shows 110 F/g and after 10000 cycles, about 73% retention. Saraf *et al.* [9] reported that $ZnFe_2O_4$/GCE microspheres express a specific capacitance of 175 F/g and 82.75% capacitance retention after 1000 cycles. Ternary transition metal ferrites, incorporating three metal elements, exhibit remarkable properties like high specific capacitance and efficient charge transfer, offering great promise for cost-effective, durable and high-performance supercapacitors in next-generation energy storage systems [10,11].

These transition metal oxides were synthesized using a variety of processes, including co-precipitation [12], hydrothermal [6,8], solvothermal [9] and wet chemical [11] procedures. Each approach enables modifications in particle size, shape and composition, making them suitable for diverse appli-

cations. In such techniques, sol-gel auto combustion is a fast, cost-effective method for synthesizing active material to supercapacitor electrodes, enabling high surface area, optimized porosity and excellent conductivity for improved energy storage and performance [10,13]. Khairy *et al.* [14] reported the CuCoF electrode exhibited a specific capacitance of 220 F/g and ~94% capacitance retention after 1000 cycles. Similarly, the electrochemical performance of the $Co_{0.5}Zn_{0.5}Fe_2O_4$ electrode and reported a specific capacitance of 218 F/g is also documented.

In this experimental study, the effects of gradually replacing Zn with Co on the structural, functional, morphological and electrochemical properties of $Co_xZn_{1-x}Fe_2O_4$ nanoparticles was investigated. The subsequent investigations aim to examine the impact of different Zn-Co ratios on their performance and properties in supercapacitor applications.

EXPERIMENTAL

Nickel(II) nitrate nonahydrate (98%, Merck), cobalt(II) nitrate hexahydrate (98%, Merck), zinc(II) nitrate hexahydrate (97%, Sigma-Aldrich) were used as received.

For the synthesis of $Co_xZn_{1-x}Fe_2O_4$ (x = 0, 0.25, 0.5) nanoparticles, $Fe(NO_3)_3{\cdot}9H_2O$, $Zn(NO_3)_2{\cdot}6H_2O$, $Co(NO_3)_2{\cdot}6H_2O$ and surfactant material (citric acid, $C_6H_8O_7$) were dissolved in deionized water separately and added together one by one. Brown sol is formed by dropwise addition of NH_3 solution such that the solution maintains a pH value of 7. For the combustion process, the temperature was increased to 120 ºC on a hot plate with continuous stirring, transforming the sol into a viscous gel. The resulting gel underwent an auto-combustion reaction, producing a loose ash-like powder. After combustion, samples were dried in an oven at 150 ºC for 90 min to remove water molecules. Further, the samples were ground and annealed at 700 ºC for 5 h.

Characterization: Rigaku MiniFlex 600 (Japan) powder Xray diffraction (p-XRD) instrument was used to determine the phase of the prepared spinel $Co_xZn_{1-x}Fe_2O_4$ (x = 0, 0.25, 0.5) solid solutions. The 2θ values in the range of 10 to 80º were used to calculate lattice constants and crystallite size. The FTIR spectra were acquired at room temperature using a Perkin-Elmer spectrometer in the 4000-400 cm^{-1} wavenumber range. Raman spectra were collected at room temperature using a commercial Confocal Raman Microscope with AFM (WiTec Alpha 300). While the spectra were obtained from 50 to 4000 cm^{-1}, this research focuses on the 200-800 cm^{-1} region. The morphological and elemental characterization of nanoparticles were done by a FEI-Quanta FEG 200F. The electrochemical studies were taken using SAS Origalys, OrigaFlex-OGF01A.

Electrode preparation: The working electrodes were prepared by mixing a slurry consisting of 80 wt.% active material, 5 wt.% polytetrafluoroethylene (PTFE) and 15 wt.% conductive carbon, along with a few drops of N-methyl-2-pyrrolidone (NMP) solution. The resulting slurry was coated onto a 1 cm × 1 cm graphite sheet using the drop-casting technique and then vacuum-dried at 60 ºC overnight. Pt-wire and Ag/AgCl electrodes act as counter electrodes and reference electrodes in three-electrode system, respectively. The electrochemical studies were carried out in 2 M Na_2SO_4 electrolytes at room temperature.

RESULTS AND DISCUSSION

XRD studies: Fig. 1 shows the Powder X-ray diffraction (PXRD) patterns of $Co_xZn_{1-x}Fe_2O_4$ (x = 0, 0.25, 0.5) nanoparticles exhibit distinct peaks at 2θ values of 29.9º, 35.2º, 37.1º, 42.8º, 53.2º, 56.6º and 62.2º. These peaks correspond to the (220), (311), (222), (400), (422), (511) and (440) planes confirm the formation of a cubic spinel ferrite structure. Among these, the (311) plane is the most intense, indicating the high crystallinity of the spinal phase. This matches well with the standard JCPDS data card no. 22-1012 corresponding to the *Fd3m* space group. The XRD pattern confirms the formation of pure and cobalt-substituted zinc ferrite and the intensity changes caused by the incorporation of cobalt into the zinc ferrite system are observed in Fig. 1. The intensities of the (220) and (440) planes are highly sensitive to the spinel ferrite system [15]. The average crystallite size can be calculated using the Debye-Scherrer's formula:

$$D = \frac{K\lambda}{\beta\cos\theta}$$

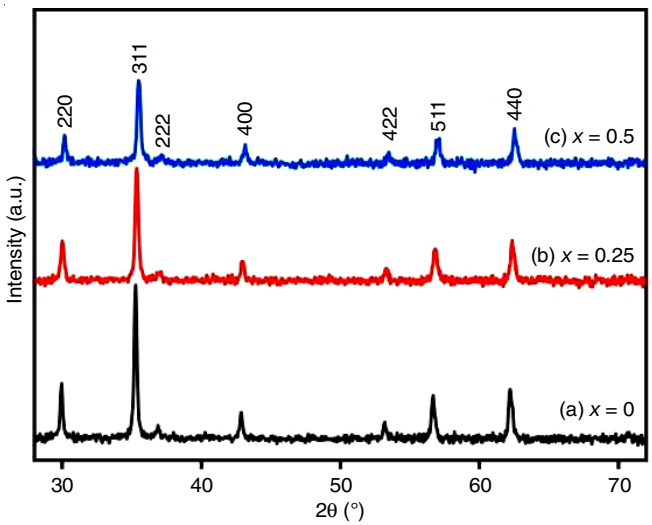

Fig. 1. XRD patterns of $Co_xZn_{1-x}Fe_2O_4$ (x = 0, 0.25, 0.5) nanoparticles

The results show a decrease in the average crystallite size (from 31.45 nm to 26.13 nm) due to the substitution of cobalt ions in the zinc-ferrite structure. The lattice constant of each peak of each sample was calculated using the following formula:

$$a = d\sqrt{(h^2 + k^2 + l^2)}$$

here, a is the lattice parameter; d is interplanar spacing which is determined using Bragg's law and h, k, l are the Miller indices [16]. The cobalt substitution is responsible for the significant decrease in the lattice constant (Table-1). The unit cell volume is calculated based on the lattice parameter.

$$V = a^3$$

FTIR studies: Fig. 2 shows the FTIR spectra cobalt-substituted zinc ferrites (x = 0, 0.25, 0.5) exhibited two prominent absorption bands, with the high-frequency band (ν_1) shifting

TABLE-1
XRD PATTERNS FOR $Co_xZn_{1-x}Fe_2O_4$ (x = 0, 0.25, 0.5) NANOPARTICLES

Sample	a (Å)	V (Å)	D (nm)
x = 0	8.431	599.402	33.726
x = 0.25	8.413	595.549	27.846
x = 0.5	8.381	588.747	26.450

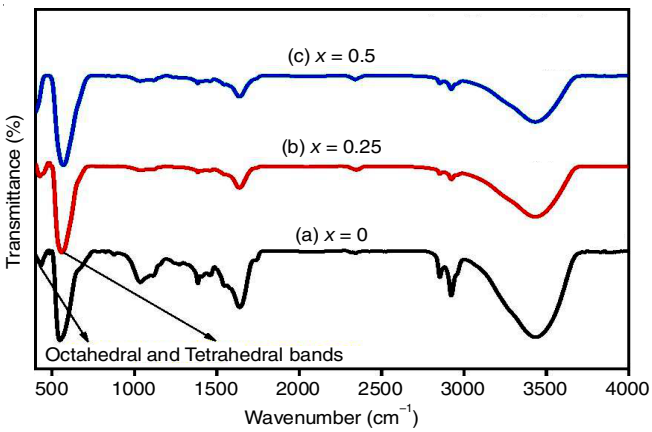

Fig. 2. FTIR spectra for $Co_xZn_{1-x}Fe_2O_4$ (x = 0, 0.25, 0.5) nanoparticles

from 546 cm^{-1} to 569 cm^{-1} and the lower-frequency band (ν_2) decreasing from 432 cm^{-1} to 402 cm^{-1}. Since these bands correspond to metal-oxygen vibrations in the tetrahedral and octahedral sites, respectively this confirms the formation of the spinel phase. The observed decrease in ν_2 and increase in ν_1 with increasing cobalt content indicate modifications changes in the metal-oxygen vibrational modes, affecting both the tetrahedral and octahedral sites [12].

Raman studies: Raman spectra of the synthesized $Co_xZn_{1-x}Fe_2O_4$ nanoparticles, as shown in Fig. 3, contains six broad peaks, $F_{2g}(1)$, E_g, $F_{2g}(2)$, $F_{2g}(3)$, $A_{1g}(2)$ and $A_{1g}(1)$ [17]. These values are given in Table-2. The $F_{2g}(1)$ mode involves the tetrahedral metal-oxygen translation, E_g corresponds to symmetric oxygen bending and $A_{1g}(1,2)$ modes arise from the symmetric oxygen stretching in AO_4 tetrahedra. $F_{2g}(2)$ and $F_{2g}(3)$ represent asymmetric stretching and bending of octahedral metal-oxygen bonds, respectively, a key feature of spinel ferrites. These modes confirm the spinel structure of the synthesized $Co_xZn_{1-x}Fe_2O_4$ nanoparticles and the structural changes caused by the incorporation of Co into the $ZnFe_2O_4$ lattice.

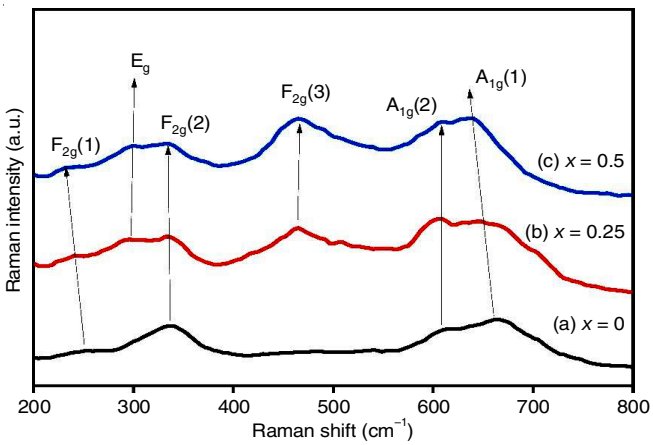

Fig. 3. Raman spectra for $Co_xZn_{1-x}Fe_2O_4$ (x = 0, 0.25, 0.5) nanoparticles

TABLE-2
RAMAN SPECTRA VALUES FOR
$Co_xZn_{1-x}Fe_2O_4$ (x = 0, 0.25, 0.5) NANOPARTICLES

Samples	$F_{2g}(1)$	E_g	$F_{2g}(2)$	$F_{2g}(3)$	$A_{1g}(2)$	$A_{1g}(1)$
x = 0	248.19	–	337.69	–	609.58	663.68
x = 0.25	241.08	293.78	333.58	464.43	604.48	651.49
x = 0.5	232.50	298.88	332.58	466.42	605.47	638.18

FESEM analysis: The field emission scanning electron microscopy (FESEM) analysis of $Co_{0.5}Zn_{0.5}Fe_2O_4$ nanoparticles, as depicted in Fig. 4a-b, reveals that the nanoparticles exhibit an agglomerate with a spherical shape. The observed morphology of the synthesized nanoparticles significantly influences their electrochemical performance. Furthermore, the EDX spectra, shown in Fig. 4c, confirms the elemental composition of the synthesized nanoparticles, verifying the presence of cobalt (Co), zinc (Zn), iron (Fe) and oxygen (O). Fig. 4d shows that the elemental ratios obtained from EDX analysis follow a stoichiometric composition of Co-Zn:Fe is 1:2, indicating the effective substitution of cobalt into the zinc ferrite structure.

Electrochemical analysis

Cyclic voltammetry (CV): The CV studies were conducted on the synthesized electrode materials at scan rates ranging from 5 to 100 mV/s. As shown in Fig. 5a-c, the increasing scan rate with specific capacitance decreases. At low scan rates, electrolyte ions fully diffuse into electrode nanopores, enabling efficient charge storage and at high scan rates, limited ion diffusion reduces capacitance. The CV curves exhibit a quasi-rectangular shape, suggest a charge storage mechanism involving both electrostatic adsorption (EDLC) and Faradaic redox reactions (pseudocapacitance). In Fig. 5a-c, the area of the curve increases due to cobalt replacement in the zinc ferrite system, which increases the specific capacity. This charge storage mechanism can be confirmed and calculated by the Dunn method [18].

Generally, the energy storage process mainly involves two parts: a non-Faradaic surface interaction with electric double-layer ion adsorption and a diffusion-controlled Faradaic reaction. The current (i) follows the power law:

$$i = av^b$$

The b value from the slope in Fig. 6a indicates the charge storage mechanism: b = 1 suggests capacitive behaviour, while b = 0.5 indicates diffusion-controlled redox. The b-values of $Co_xZn_{1-x}Fe_2O_4$ (x = 0, 0.25, 0.5) are 0.63, 0.66 and 0.69, respectively, revealing a transition from diffusion-controlled to capacitive processes. The total stored charge contributions can be expressed as:

$$i(V) = k_1\nu + k_2\nu^{1/2}$$

where $k_1\nu$ represents capacitive effects and $k_2\nu^{1/2}$ corresponds to diffusion-controlled processes.

Fig. 6b-d illustrates the capacitive and diffusion-controlled charge contributions for $Co_xZn_{1-x}Fe_2O_4$ (x = 0, 0.25, 0.5) electrodes. Diffusion-controlled charges dominate the total charge at low scan rates, whereas at higher scan rates, the capacitive contributions dominate. Increasing Co content enhances the capacitive contribution, making the material more suitable for high-power supercapacitor applications [19,20].

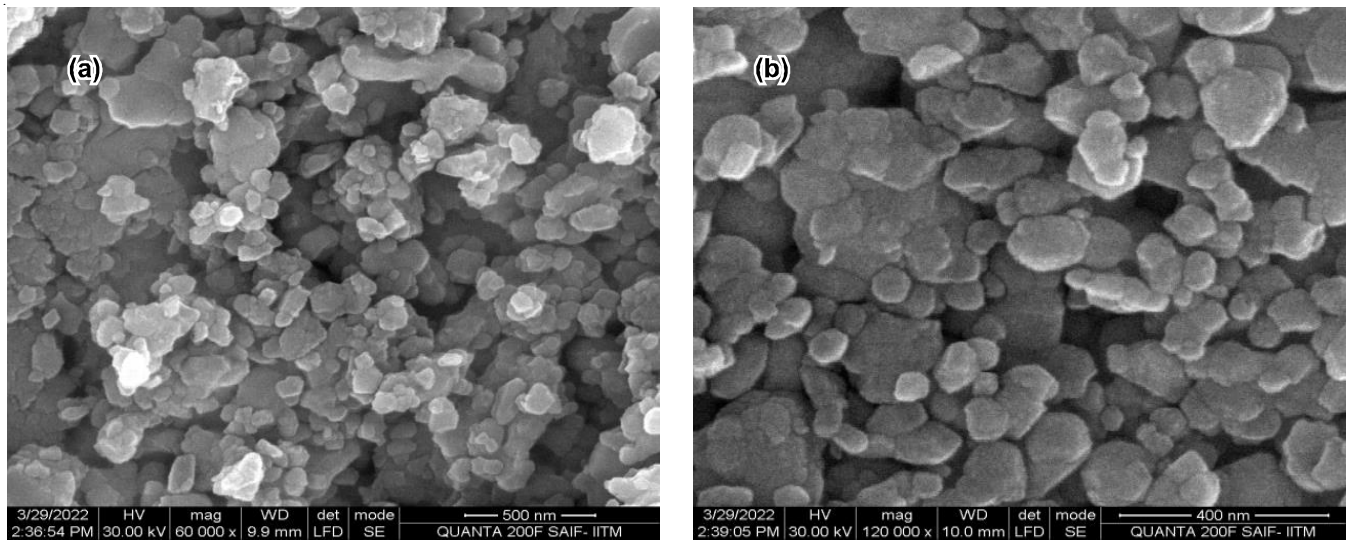

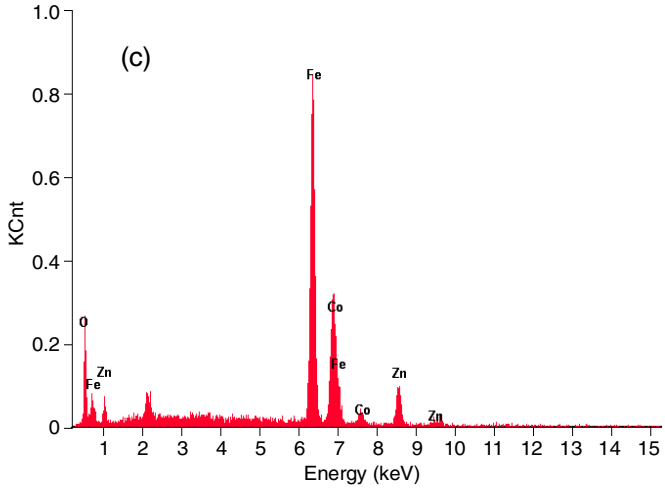

(d)

Element	Weight (%)	Atomic (%)
OK	17.50	43.43
FeK	49.16	34.95
CoK	20.48	13.80
ZnK	12.87	7.82
Matrix	Correction	ZAF

Fig. 4. (a-b) FESEM images of $Co_{0.5}Zn_{0.5}Fe_2O_4$, (c-d) EDX image and wt.% of elements of $Co_{0.5}Zn_{0.5}Fe_2O_4$

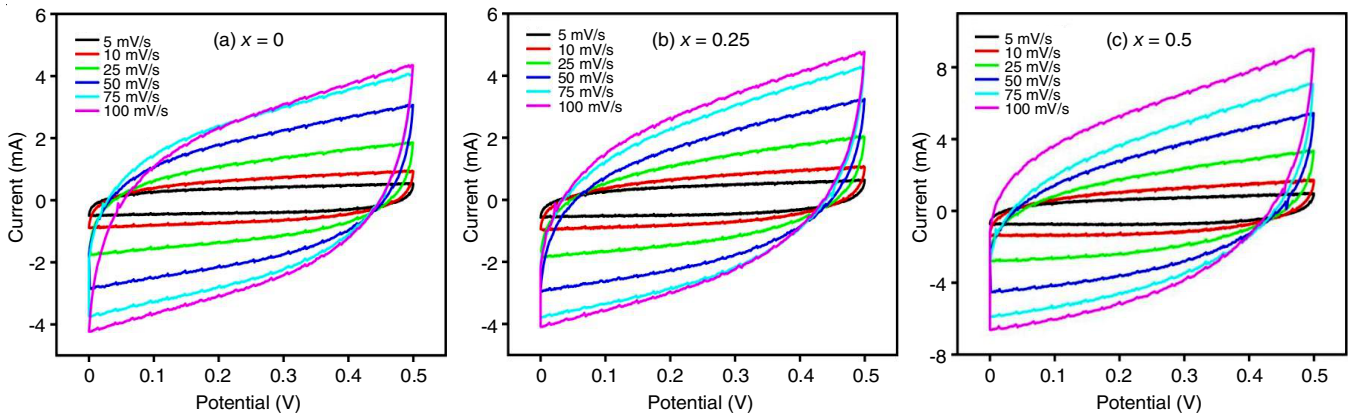

Fig. 5. Cyclic voltammograms for $Co_xZn_{1-x}Fe_2O_4$ (x = 0, 0.25, 0.5) electrodes

GCD analysis: The GCD curves of $Co_xZn_{1-x}Fe_2O_4$ (x = 0, 0.25, 0.5) electrodes recorded at different current densities ranging from 1 to 10 A/g, are shown in Fig. 7a-c. The GCD graphs show a nearly triangular shape with a slight IR drop at the start of the discharge curve indicating low internal resistance at the electrode/electrolyte interface [21]. The specific capacitance has been calculated from the following equation:

$$C_s = \frac{I.\Delta t}{m.\Delta V}$$

where C_s (F/g) is the specific capacitance, I (A) is the applied current, Δt is discharge time, ΔV the potential window and m is the mass of the active material [22,23]. The specific capacitance values, calculated from the discharge curves at 1 A/g,

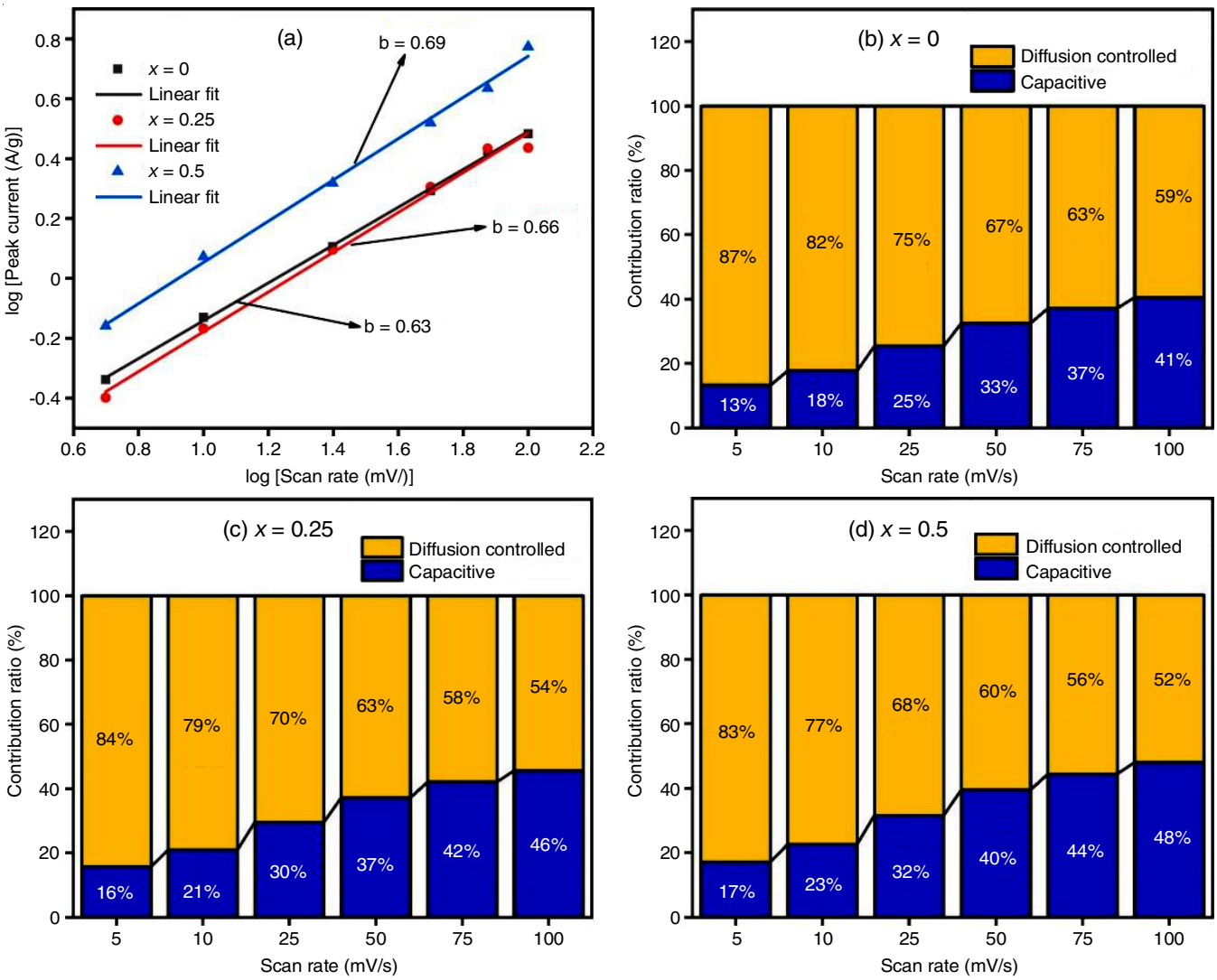

Fig. 6. (a) b values and (b-d) capacitance contribution from the Dunn method for $Co_xZn_{1-x}Fe_2O_4$ (x = 0, 0.25, 0.5) electrodes

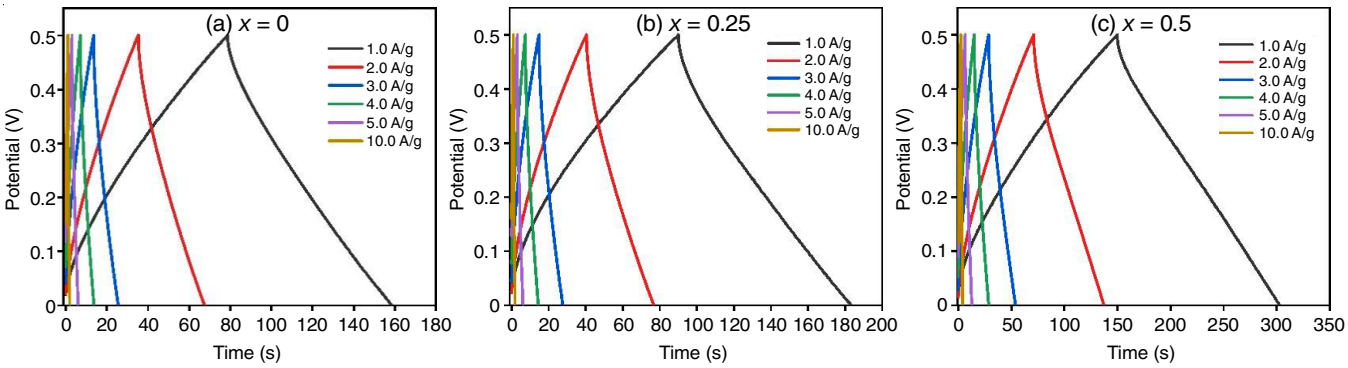

Fig. 7. GCD curves for $Co_xZn_{1-x}Fe_2O_4$ (x = 0, 0.25, 0.5) electrodes

are 159.6 F/g, 186.2 F/g and 306.2 F/g for x = 0, 0.25 and 0.5, respectively. At low current densities, longer discharge time indicates higher charge storage, while at high current densities, shorter discharge time results from limited electrolyte ion diffusion into electrode nanopores. Increasing the Co content improves conductivity, ion diffusion and the increase in specific capacitance, making the $Co_{0.5}Zn_{0.5}Fe_2O_4$ material more suitable for high-power supercapacitor applications.

Electrochemical impedance spectroscopy (EIS): The EIS is a powerful technique for analyzing the resistive properties of samples over a wide frequency range of 0.01 Hz–100 kHz. Fig. 8 represented the Nyquist plot of $Co_xZn_{1-x}Fe_2O_4$ (x = 0, 0.25, 0.5) electrodes exhibit an initial region indicates solution resistance (R_s), the semi-circle in high frequency represents charge transfer resistance (R_{ct}) and a straight line in low frequency indicates ion diffusion from the electrolyte to the electrode

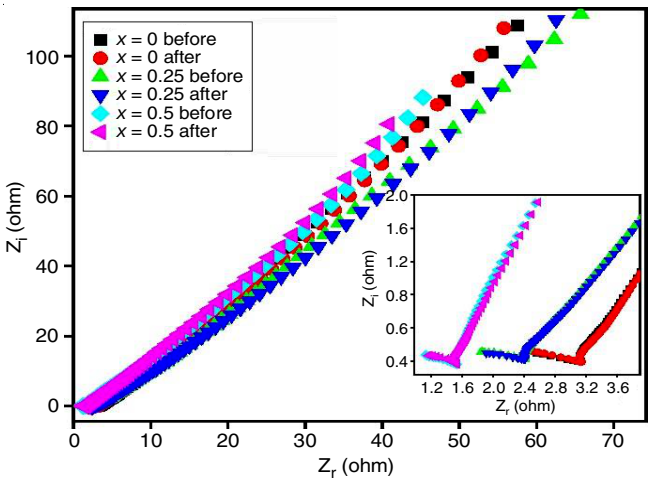

Fig. 8. Nyquist plot of $Co_xZn_{1-x}Fe_2O_4$ (x = 0, 0.25, 0.5) electrodes before and after 4000 cycles

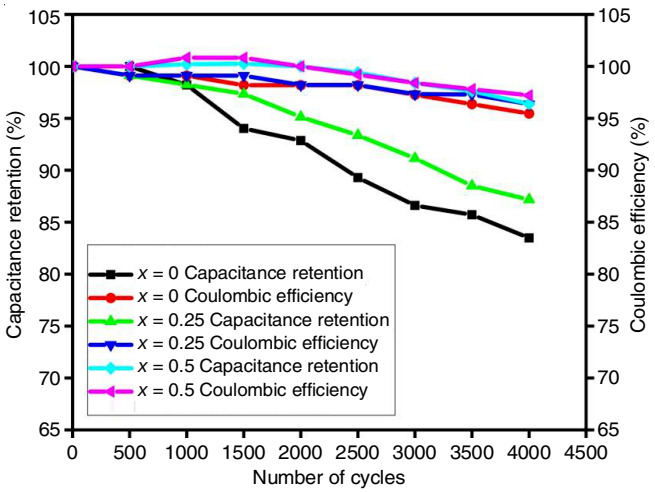

Fig. 9. Cyclic stability test (4000 cycles) for $Co_xZn_{1-x}Fe_2O_4$ (x = 0, 0.25, 0.5) electrodes

surface as Warburg impedance (W) [12]. R_{ct} values of the electrodes are before and after the stability test are shown in Table-3. These are due to the fast-Faradaic charge transfer during the electrochemical process [24]. The Nyquist plots of the cobalt-substituted zinc ferrites have low charge transfer resistance and low ion diffusion resistance, indicating better ionic conductivity, which is attributed to the increase in cobalt content.

TABLE-3
ELECTROCHEMICAL VALUES FOR SUPERCAPACITOR OF $Co_xZn_{1-x}Fe_2O_4$ (x = 0, 0.25, 0.5) NANOPARTICLES

Samples	C_s at 1 A/g (F/g)	R_{ct} before (ohm)	R_{ct} after (ohm)	Capacitance retention (%)
x = 0	159.6	0.71	0. 68	83.5
x = 0.25	186.2	0.56	0.49	87.2
x = 0.5	306.2	0.40	0.36	96.4

Cyclic stability test: As long-term cycling stability is crucial for assessing the practical use of supercapacitor materials, $Co_xZn_{1-x}Fe_2O_4$ (x = 0, 0.25, 0.5) electrodes were tested for 4000 cycles at a current density of 10 A/g as shown in Fig. 9 and the values are given in Table-3 [23]. The $Co_{0.5}Zn_{0.5}Fe_2O_4$ electrodes demonstrate outstanding electrochemical stability, retaining 96.4% of its capacitance after 4000 cycles.

Conclusion

In present work, cobalt-substituted zinc ferrites ($Co_xZn_{1-x}Fe_2O_4$) nanoparticles have been successfully synthesized and their structural, morphological and electrochemical properties were also carried out. XRD result confirmed a cubic spinel phase with reduced crystallite size upon cobalt substitution, while FTIR and Raman spectra exhibited the metal-oxygen vibrations. FESEM and EDX studies showed agglomerated morphology and correct stoichiometry. The electrochemical analysis revealed that increasing cobalt content enhances both charge storage capacity and electrical behaviour and GCD showed a maximum conductivity. CV confirmed pseudocapacitive capacitance of 306.2 F/g at 1 A/g for $Co_{0.5}Zn_{0.5}Fe_2O_4$. EIS indicated lower charge transfer resistance and better ion diffusion. The material maintained 96% capacitance after 4000 cycles, confirming its potential as a high-performance supercapacitor electrode.

ACKNOWLEDGEMENTS

The authors are grateful to Department of Physics, Govt. Arts College (Autonomous), Nandanam, Chennai, for their support in completing this research. The authors also express their gratitude to the Government College of Engineering, Bargur and St. Joseph's College (Autonomous), Tiruchirappalli, for providing the instrumental facilities required for the material characterization.

CONFLICT OF INTEREST

The authors declare that there is no conflict of interests regarding the publication of this article.

REFERENCES

1. O. Krishan and S. Suhag, *Int. J. Energy Res.*, **43**, 6171 (2019); https://doi.org/10.1002/er.4285
2. R.T. Yadlapalli, R.R. Alla, R. Kandipati and A. Kotapati, *J. Energy Storage*, **49**, 104194 (2022); https://doi.org/10.1016/j.est.2022.104194
3. D.P. Dubal, N.R. Chodankar, D.H. Kim and P. Gomez-Romero, *Chem. Soc. Rev.*, **47**, 2065 (2018); https://doi.org/10.1039/C7CS00505A
4. M. Mortazavi and A. Ivanov, *Int. J. Adv. Manuf. Technol.*, **105**, 4621 (2019); https://doi.org/10.1007/s00170-019-03864-2
5. P.A. Shinde, Y. Seo, S. Lee, H. Kim, Q.N. Pham, Y. Won and S. Chan Jun, *Chem. Eng. J.*, **387**, 122982 (2020); https://doi.org/10.1016/j.cej.2019.122982
6. P. Gaikwad, N. Tiwari, R. Kamat, S.M. Mane and S.B. Kulkarni, *Mater. Sci. Eng. B*, **307**, 117544 (2024); https://doi.org/10.1016/j.mseb.2024.117544
7. Q. Luo, P. Xu, Y. Qiu, Z. Cheng, X. Chang and H. Fan, *Mater. Lett.*, **198**, 192 (2017); https://doi.org/10.1016/j.matlet.2017.04.032
8. X. Feng, Y. Huang, X. Chen, C. Wei, X. Zhang and M. Chen, *J. Mater. Sci.*, **53**, 2648 (2018); https://doi.org/10.1007/s10853-017-1735-9
9. M. Saraf, K. Natarajan, A.K. Gupta, P. Kumar, R. Rajak and S.M. Mobin, *Mater. Res. Express*, **6**, 095534 (2019); https://doi.org/10.1088/2053-1591/ab3339
10. Y. Lin, J. Wang, H. Yang, L. Wang and M. Cao, *Mater. Sci. Eng. B*, **228**, 103 (2018); https://doi.org/10.1016/j.mseb.2017.11.013

11. N.M. Malima, M.D. Khan, J. Choi, R.K. Gupta, P. Mashazi, T. Nyokong and N. Revaprasadu, *RSC Adv.*, **11**, 31002 (2021); https://doi.org/10.1039/D1RA04833C
12. B.J. Rani, G. Ravi, R. Yuvakkumar, V. Ganesh, S. Ravichandran, M. Thambidurai, A.P. Rajalakshmi and A. Sakunthala, *Appl. Phys., A Mater. Sci. Process.*, **124**, 511 (2018); https://doi.org/10.1007/s00339-018-1936-3
13. A. Sutka and G. Mezinskis, *Front. Mater. Sci.*, **6**, 128 (2012); https://doi.org/10.1007/s11706-012-0167-3
14. M. Khairy, W.A. Bayoumy, S.S. Selima and M.A. Mousa, *J. Mater. Res.*, **35**, 2652 (2020); https://doi.org/10.1557/jmr.2020.200
15. N.M. Deraz and A. Alarifi, *J. Anal. Appl. Pyrolysis*, **94**, 41 (2012); https://doi.org/10.1016/j.jaap.2011.10.004
16. K.J. Oviya and P. Sivagurunathan, *Asian J. Chem.*, **36**, 2375 (2024); https://doi.org/10.14233/ajchem.2024.32404
17. S. Demirel, R. Topkaya and K. Cicek, *J. Mater. Sci. Mater. Electron.*, **34**, 1 (2023); https://doi.org/10.1007/s10854-022-09392-2
18. V. Augustyn, J. Come, M.A. Lowe, J.W. Kim, P.L. Taberna, S.H. Tolbert, H.D. Abruña, P. Simon and B. Dunn, *Nature Mater.*, **12**, 518 (2013); https://doi.org/10.1038/nmat3601
19. S. Suresh and V. Sindhu, *Ionics*, **29**, 843 (2023); https://doi.org/10.1007/s11581-022-04846-3
20. J. Wang, J. Polleux, J. Lim and B. Dunn, *J. Phys. Chem. C*, **111**, 14925 (2007); https://doi.org/10.1021/jp074464w
21. B. Bhujun, M.T. Tan and A.S. Shanmugam, *Results Phys.*, **7**, 345 (2017); https://doi.org/10.1016/j.rinp.2016.04.010
22. T. Putjuso, S. Putjuso, A. Karaphun, P. Moontragoon, I. Kotutha and E. Swatsitang, *Sci. Rep.*, **13**, 2531 (2023); https://doi.org/10.1038/s41598-023-29830-3
23. L. Li, H. Bi, S. Gai, F. He, P. Gao, Y. Dai, X. Zhang, D. Yang, M. Zhang and P. Yang, *Sci. Rep.*, **7**, 43116 (2017); https://doi.org/10.1038/srep43116
24. P.D. Patil, S.R. Shingte, V.C. Karade, J.H. Kim, T.D. Dongale, S.H. Mujawar, A.M. Patil and P.B. Patil, *J. Energy Storage*, **40**, 102821 (2021); https://doi.org/10.1016/j.est.2021.102821